

Research Article

Oblique Incidence of Seismic Wave Reflecting Two Components of Design Ground Motion

W. J. Cen ^{1,2}, X. H. Du,¹ D. J. Li,¹ and L. N. Yuan¹

¹College of Water Conservancy and Hydropower Engineering, Hohai University, Nanjing, Jiangsu 210098, China

²Yangtze River Scientific Research Institute, Wuhan 430010, China

Correspondence should be addressed to W. J. Cen; hhucwj@163.com

Received 21 February 2018; Accepted 24 April 2018; Published 13 June 2018

Academic Editor: Lutz Auersch

Copyright © 2018 W. J. Cen et al. This is an open access article distributed under the Creative Commons Attribution License, which permits unrestricted use, distribution, and reproduction in any medium, provided the original work is properly cited.

The wave field on the artificial boundary was separated into the free field without local topography effect and scattering field induced by local topography effect. The simulation of the free field under obliquely incident waves was conducted. Based on the assumption that the components of design ground motion were treated as the coincidence of oblique P wave and oblique SV wave, the relationship between the oblique input waves and the design ground motion was established in the free field. Further, the contributions to the two components of design ground motion of obliquely incident waves were discussed. The calculation model in time domain was achieved by the combination of the propagation characteristics of obliquely incident waves and the artificial boundary in the free field. The seismic response to the design ground motion was produced on the free surface. The verification of the 2D half-space model under oblique input waves indicated that the wave input method can accurately reflect the design ground motion on the free surface. Application of an earth-rock dam showed that oblique incidence of seismic waves results in significantly different dynamic response compared with the normal incidence. The proposed method can also be employed in the seismic analysis of large span structures with nonuniform ground motion input.

1. Introduction

Due to uncertainties of seismic ground motion input and complexity of dynamic response, the seismic safety of large-scale structures (e.g., high dams) is widely concerned. For the analysis of seismic response, it is generally assumed that all points on the interface between the structure and foundation are subjected to the earthquake excitation with the same phase [1–4]. Actually, the earthquake input at the bottom of the structure is not entirely consistent for different propagation routes of seismic wave, different local site conditions, and the interaction between structure and foundation. As a consequence, it is of importance to study the seismic input method reflecting the characteristics of the spatial variation for large-scale structures.

In order to ensure the security of large-scale structures under the action of near-field earthquake, the reasonable seismic input method is the vital basis of accurate seismic analysis. For external source wave motion problem such as seismic wave problem, the effect of near-field wave motion

is always focused on. Therefore, the limited treatment to the infinite continuum is performed and the artificial boundary in the medium is factitiously introduced. The artificial boundary can reduce the reflection of the outward traveling waves and is imposed to simulate the energy radiation effect at the truncation of an infinite domain. Due to the high precision of viscous-spring artificial boundary, the seismic input method can be used by combining the viscous-spring artificial boundary with wave field decomposition technique [5]. The wave field on an artificial boundary is separated into the free field without local topography effect and scattering field induced by local topography effect [6]. Meanwhile, the analysis model of the free field is established to realize the numerical simulation of external source wave motion problem. The free field with obliquely incident waves can be simulated in the frequency domain, but the approach simulating the free field in frequency domain needs much computational effort and large storage capacity. Consequently, the adaptable and convenient time-domain method with high accuracy was highly recommended [7, 8]. Based on the

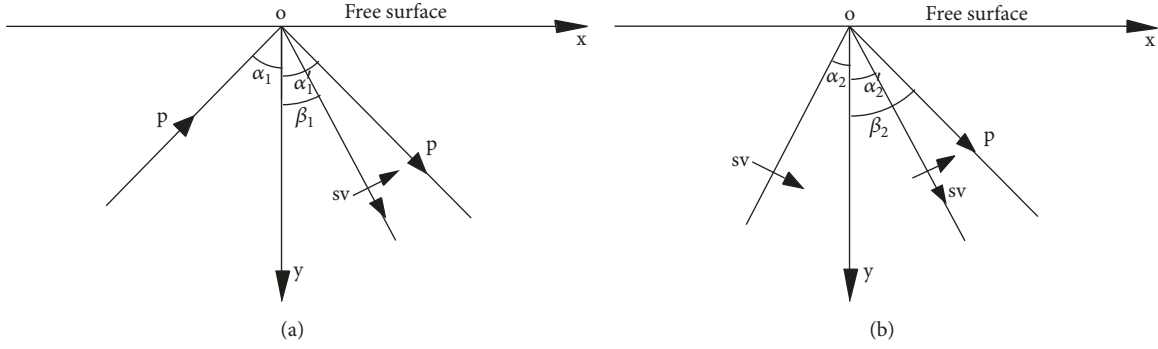


FIGURE 1: Reflection of obliquely incident waves on the free surface: (a) P wave and (b) SV wave.

viscous-spring artificial boundary model, the input boundary was adjusted to be consistent with the oscillation face by Wu [9]. The oblique incidence was converted into the normal incidence, and the nonsynchronous wave was converted into the synchronous wave. The incidence orientation that has the most serious influence on earth dam stability was presented based on the input method of seismic motion.

The seismic response analysis of the structures mentioned above was based on the case that the input wave was definite in free field. Although the input wave has some connection with the design ground motion on the free surface, it cannot entirely reflect the nature of the ground motion that the engineered structure site will be encountered in the future [10, 11]. To establish oblique incident wave field reflecting the design ground motion, the oblique plane SV wave and oblique plane P wave were developed from the one-way ground motion on the free surface [12]. However, only considering the oblique plane waves from the one-way ground motion cannot reflect the real situation of ground motion. In this paper, the oblique SV wave and oblique P wave were obtained by synthetically considering the horizontal and vertical ground motions on the free surface. The seismic response of the half-space model was the same as the design seismic component on the free surface when the obliquely incident waves were input simultaneously. The method of oblique input waves reflecting two components of design ground motion was established using the viscous-spring artificial boundary.

2. Free Field with Obliquely Incident Waves

According to the theory of wave propagation in solid [13], reflective waves consist of P wave and SV wave when the oblique P wave and SV wave reach the free surface of half-space, as shown in Figure 1. The relationship among the incident, reflected, and transmitted angles upon the single interface can be determined by Snell's law.

Figure 1 shows the coordinate system for incident waves, where x -axis and y -axis are the horizontal and vertical directions, respectively; α_1 is the incident angle of P wave, and α_2 is the incident angle of SV wave; α'_1 is the angle of the reflected plane P wave, and α'_2 is the angle of the reflected plane SV wave; v_p and v_s are the velocities of P wave and SV wave, respectively.

When the incidence of P wave occurs, the reflection coefficients of reflected P wave and reflected SV wave are represented by A_1 and A_2 , respectively [14]. In the case of the incident SV wave, the reflection coefficients of reflected P wave and reflected SV wave are represented by A'_1 and A'_2 , respectively [15]. According to Snell's law and stress equilibrium conditions on the free surface, the reflection coefficients are presented as follows:

$$\begin{aligned}
 A_1 &= \frac{v_s^2 \sin 2\alpha_1 \sin 2\beta_1 - v_p^2 \cos^2 2\beta_1}{v_p^2 \sin 2\alpha_1 \sin 2\beta_1 + v_s^2 \cos^2 2\beta_1} \\
 A_2 &= \frac{2v_p v_s \sin 2\alpha_1 \cos 2\beta_1}{v_s^2 \sin 2\alpha_1 \sin 2\beta_1 + v_p^2 \cos^2 2\beta_1} \\
 A'_1 &= \frac{2v_p v_s \sin 2\alpha_2 \cos 2\alpha_2}{v_s^2 \sin 2\alpha_2 \sin 2\beta_2 + v_p^2 \cos^2 2\beta_2} \\
 A'_2 &= \frac{-v_s^2 \sin 2\alpha_2 \sin 2\beta_2 + v_p^2 \cos^2 2\alpha_2}{v_s^2 \sin 2\alpha_2 \sin 2\beta_2 + v_p^2 \cos^2 2\beta_2}
 \end{aligned} \tag{1}$$

Herein, the motion of P wave in the free field is expressed by $u(x, y, t)$. When the oblique input P wave propagates the distance r with the incident angle α as shown in Figure 2, the incident wave field and the reflected wave field of a node (x, y) in the half-space can be expressed by the following equations:

$$\begin{aligned}
 u_x^{(0)}(x, y, t) &= u \left(t - \frac{r}{v_p} \right) \sin \alpha_1 \\
 u_y^{(0)}(x, y, t) &= -u \left(t - \frac{r}{v_p} \right) \cos \alpha_1 \\
 u_x^{(1)}(x, y, t) &= A_1 u \left(t - \frac{r}{v_p} \right) \sin \alpha'_1 \\
 u_y^{(1)}(x, y, t) &= A_1 u \left(t - \frac{r}{v_p} \right) \cos \alpha'_1 \\
 u_x^{(2)}(x, y, t) &= A_2 u \left(t - \frac{r}{v_s} \right) \cos \beta_1 \\
 u_y^{(2)}(x, y, t) &= -A_2 u \left(t - \frac{r}{v_s} \right) \sin \beta_1
 \end{aligned} \tag{2}$$

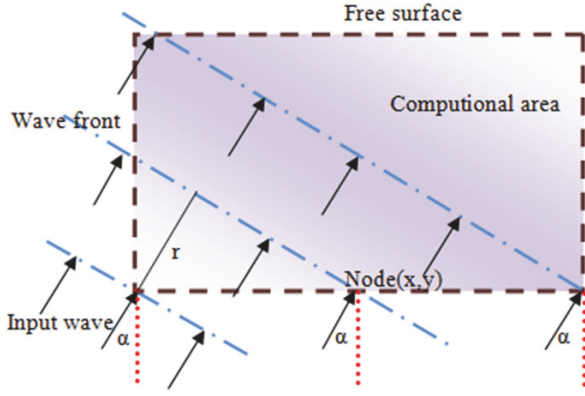


FIGURE 2: Free field with the obliquely incident wave.

where $u_x^{(0)}(x, y, t)$ and $u_y^{(0)}(x, y, t)$ are the horizontal and vertical incident wave fields of incident P wave, respectively; $u_x^{(1)}(x, y, t)$ and $u_y^{(1)}(x, y, t)$ are the horizontal and vertical wave fields of reflected P wave, respectively; $u_x^{(2)}(x, y, t)$ and $u_y^{(2)}(x, y, t)$ are the horizontal and vertical wave fields of reflected SV wave, respectively.

When the incident SV wave is determined, the incident wave field and the reflected wave field of a node (x, y) in the half-space can be expressed as

$$\begin{aligned}
 u_x^{(0)}(x, y, t) &= u \left(t - \frac{r}{v_s} \right) \cos \alpha_2 \\
 u_y^{(0)}(x, y, t) &= u \left(t - \frac{r}{v_s} \right) \sin \alpha_2 \\
 u_x^{(1)}(x, y, t) &= A_1 u \left(t - \frac{r}{v_p} \right) \sin \beta_2 \\
 u_y^{(1)}(x, y, t) &= A_1 u \left(t - \frac{r}{v_p} \right) \cos \beta_2 \\
 u_x^{(2)}(x, y, t) &= A_2 u \left(t - \frac{r}{v_s} \right) \cos \alpha'_2 \\
 u_y^{(2)}(x, y, t) &= -A_2 u \left(t - \frac{r}{v_s} \right) \sin \alpha'_2
 \end{aligned} \tag{3}$$

where $u_x^{(0)}(x, y, t)$ and $u_y^{(0)}(x, y, t)$ are the horizontal and vertical incident wave fields of SV wave, respectively; $u_x^{(1)}(x, y, t)$ and $u_y^{(1)}(x, y, t)$ are the horizontal and vertical wave fields of reflected P wave, respectively; $u_x^{(2)}(x, y, t)$ and $u_y^{(2)}(x, y, t)$ are the horizontal and vertical wave fields of reflected SV wave, respectively.

The incident plane SV wave meets Snell's law and there exists a critical incident angle as

$$\alpha_{cr} = \sin^{-1} \left(\frac{v_s}{v_p} \right) \tag{4}$$

When $\alpha_2 > \alpha_{cr}$, the relation $\sin \alpha'_2 = (v_p/v_s) \sin \alpha_2$ will have no real-valued solution for the angle α'_2 , and the reflective waves are not plane waves but nonuniform waves. Since the characteristics of nonuniform waves are different from plane waves, only the case of $\alpha_2 \leq \alpha_{cr}$ is investigated in this study.

3. Obliquely Incident Waves Reflecting the Design Ground Motion

Assuming that point $O(0,0)$ on the free surface of half-space is the reference point, the horizontal and vertical components of the design seismic motion of the reference point are represented by $u_h(t)$ and $u_v(t)$, respectively. The incident P wave and the incident SV wave are constructed at the reference point $O(0,0)$. When P wave and SV wave are input with an incident angle simultaneously at the artificial boundary, the same seismic response is produced to that of the design seismic component on the free surface. Thus, the horizontal and vertical components can be defined as [13, 16]

$$\begin{aligned}
 u_h(t) &= u_x^{(0)}(t) + u_x^{(1)}(t) + u_x^{(2)}(t) \\
 u_v(t) &= u_y^{(0)}(t) + u_y^{(1)}(t) + u_y^{(2)}(t)
 \end{aligned} \tag{5}$$

By substituting (2) and (3) into (5), it can be expressed as

$$\begin{aligned}
 u_h(t) &= g \left(t - \frac{x \sin \alpha_1 - y \cos \alpha_1}{v_p} \right) \sin \alpha_1 \\
 &+ A_1 g_1 \left(t - \frac{x \sin \alpha'_1 + y \cos \alpha'_1}{v_p} \right) \sin \alpha'_1 \\
 &+ A_2 g_2 \left(t - \frac{x \sin \beta_1 + y \cos \beta_1}{v_s} \right) \cos \beta_1 \\
 &+ f \left(t - \frac{x \sin \alpha_2 - y \cos \alpha_2}{v_s} \right) \cos \alpha_2 \\
 &+ A'_1 f_1 \left(t - \frac{x \sin \beta_2 + y \cos \beta_2}{v_p} \right) \sin \beta_2 \\
 &+ A'_2 f_2 \left(t - \frac{x \sin \alpha'_2 + y \cos \alpha'_2}{v_s} \right) \cos \alpha'_2 \\
 u_v(t) &= -g \left(t - \frac{x \sin \alpha_1 - y \cos \alpha_1}{v_p} \right) \cos \alpha_1 \\
 &+ A_1 g_1 \left(t - \frac{x \sin \alpha'_1 + y \cos \alpha'_1}{v_p} \right) \cos \alpha'_1 \\
 &- A_2 g_2 \left(t - \frac{x \sin \beta_1 + y \cos \beta_1}{v_s} \right) \sin \beta_1 \\
 &+ f \left(t - \frac{x \sin \alpha_2 - y \cos \alpha_2}{v_s} \right) \sin \alpha_2
 \end{aligned} \tag{6}$$

$$\begin{aligned}
& + A'_1 f_1 \left(t - \frac{x \sin \beta_2 + y \cos \beta_2}{v_p} \right) \cos \beta_2 \\
& - A'_2 f_2 \left(t - \frac{x \sin \alpha'_2 + y \cos \alpha'_2}{v_s} \right) \sin \alpha'_2
\end{aligned} \quad (7)$$

For the nodes on the free surface ($y = 0$), (6) and (7) can be expressed as follows according to Snell's law [16]:

$$\begin{aligned}
u_h(t) &= g \left(t - \frac{x \sin \alpha_1}{v_p} \right) \\
&\cdot (\sin \alpha_1 + A_1 \sin \alpha'_1 + A_2 \cos \beta_1)
\end{aligned} \quad (8)$$

$$\begin{aligned}
& + f \left(t - \frac{x \sin \alpha_2}{v_s} \right) (\cos \alpha_2 + A'_1 \sin \beta_2 + A'_2 \cos \alpha'_2) \\
u_v(t) &= g \left(t - \frac{x \sin \alpha_1}{v_p} \right) \\
&\cdot (-\cos \alpha_1 + A_1 \cos \alpha'_1 - A_2 \sin \beta_1) \\
& + f \left(t - \frac{x \sin \alpha_2}{v_s} \right) (\sin \alpha_2 + A'_1 \cos \beta_2 - A'_2 \sin \alpha'_2)
\end{aligned} \quad (9)$$

The incident angle should meet (10) to make (8) and (9) reasonable when the oblique input waves are simultaneously transmitted to the free surface.

$$\frac{\sin \alpha_1}{v_p} = \frac{\sin \alpha_2}{v_s} \quad (10)$$

The horizontal and vertical component coefficients of oblique input waves can be defined as

$$\begin{aligned}
k_x^p &= \sin \alpha_1 + A_1 \sin \alpha'_1 + A_2 \cos \beta_1 \\
k_y^p &= -\cos \alpha_1 + A_1 \cos \alpha'_1 - A_2 \sin \beta_1 \\
k_x^{sv} &= \cos \alpha_2 + A'_1 \sin \beta_2 + A'_2 \cos \alpha'_2 \\
k_y^{sv} &= \sin \alpha_2 + A'_1 \cos \beta_2 - A'_2 \sin \alpha'_2
\end{aligned} \quad (11)$$

where k_x^p and k_x^{sv} are the horizontal component coefficients of reflected P and SV waves, respectively; k_y^p and k_y^{sv} are the vertical component coefficients of reflected P and SV waves with incident plane SV wave, respectively.

Thus, (8) and (9) can be expressed as

$$u_h(t) = g \left(t - \frac{x \sin \alpha_1}{v_p} \right) k_x^p + f \left(t - \frac{x \sin \alpha_2}{v_s} \right) k_x^{sv} \quad (12)$$

$$u_v(t) = g \left(t - \frac{x \sin \alpha_1}{v_p} \right) k_y^p + f \left(t - \frac{x \sin \alpha_2}{v_s} \right) k_y^{sv} \quad (13)$$

The incident P wave and the incident SV wave can be obtained as

$$\begin{aligned}
g \left(t - \frac{x \sin \alpha_1}{v_p} \right) &= \frac{k_y^{sv} u_h(t)}{k_x^p k_y^{sv} - k_x^{sv} k_y^p} + \frac{k_x^{sv} u_v(t)}{k_x^{sv} k_y^p - k_x^p k_y^{sv}} \\
f \left(t - \frac{x \sin \alpha_2}{v_s} \right) &= \frac{k_y^p u_h(t)}{k_x^{sv} k_y^p - k_x^p k_y^{sv}} + \frac{k_x^p u_v(t)}{k_x^p k_y^{sv} - k_x^{sv} k_y^p}
\end{aligned} \quad (14)$$

The incident wave field is determined by (14) and the seismic response at any point on the free surface is identical to the design seismic motion. Further, the incident waves can produce nonuniform motion due to the time difference for different nodes on the free surface.

The obliquely incident P and SV waves are composed of the horizontal and vertical components. The contributions to the two components of design ground motion of obliquely incident P wave are expressed by $k_y^{sv}/(k_x^p k_y^{sv} - k_x^{sv} k_y^p)$ and $k_x^{sv}/(k_x^{sv} k_y^p - k_x^p k_y^{sv})$, respectively. The contributions of obliquely incident SV wave to the two components of design seismic motion are expressed by $k_y^p/(k_x^{sv} k_y^p - k_x^p k_y^{sv})$ and $k_x^p/(k_x^p k_y^{sv} - k_x^{sv} k_y^p)$, respectively. Figures 3 and 4 show the contributions of obliquely incident P wave and SV wave, respectively.

As shown in Figures 3 and 4, when the seismic wave propagates vertically, the horizontal component on the free surface is entirely produced by SV wave, and the vertical component is entirely produced by P wave. With increasing incident angle of SV wave, the contribution of horizontal component gradually decreases, and the vertical component progressively increases. In contrast to incident SV wave, the contribution of horizontal component gradually increases, while the contribution of the vertical component progressively increases for P wave. When the incident angle of incident P wave is 90° , true waves horizontally propagate on the ground surface. With increasing depth into the half-space away from the surface, the amplitude exponentially decreases [16]. Meanwhile, the density of the medium gradually increases from the surface to the bottom, and the reflection and refraction occur on the surface. When the incident wave reaches the surface, the incident angle of the input wave is always less than 90° .

4. Seismic Wave Input Method

When the finite element method is adopted to solve the problem of wave scattering in earthquake engineering, the artificial boundary is introduced to make outgoing wave motions pass through the boundary without reflection. The artificial boundaries, such as transmitting boundary [17], Clayton-Engquist boundary [18, 19], viscous boundary [20, 21], and viscous-spring boundary [22, 23], are proposed to eliminate reflection and to simulate the process of wave transmission. The transmitting boundary has high accuracy, but a certain amount of nodes and elements should be added on the boundary that needs large computing storage capacity. Further, transmitting boundary has high-frequency oscillation instability problem. Clayton-Engquist boundary is

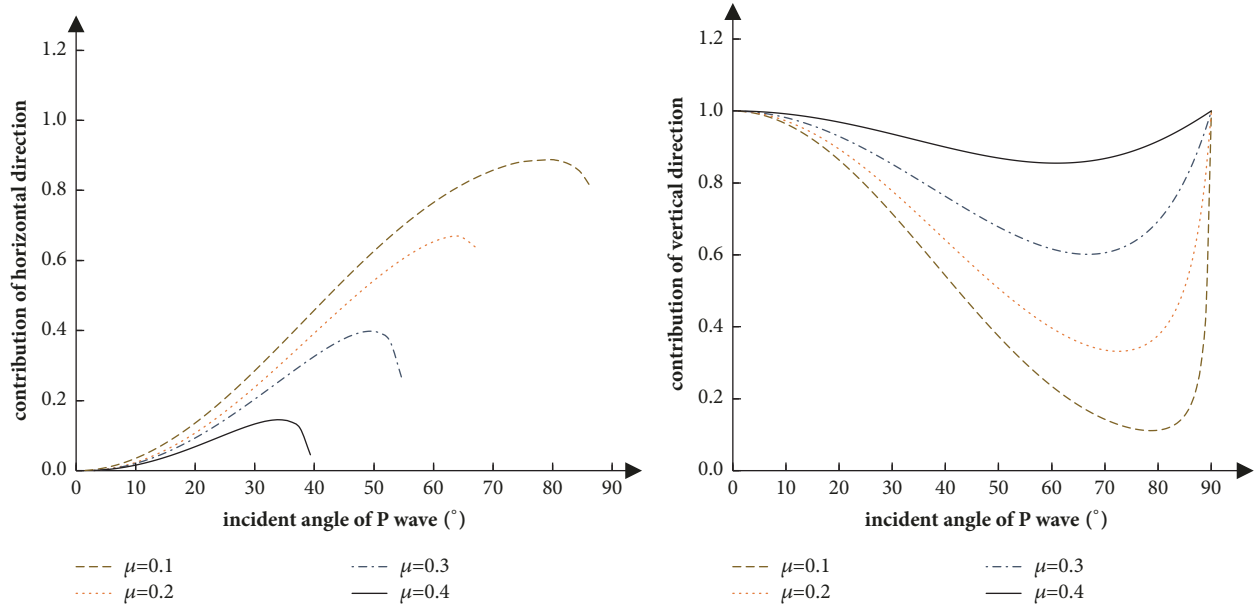


FIGURE 3: Contribution of P wave to the design ground motion on the free surface.

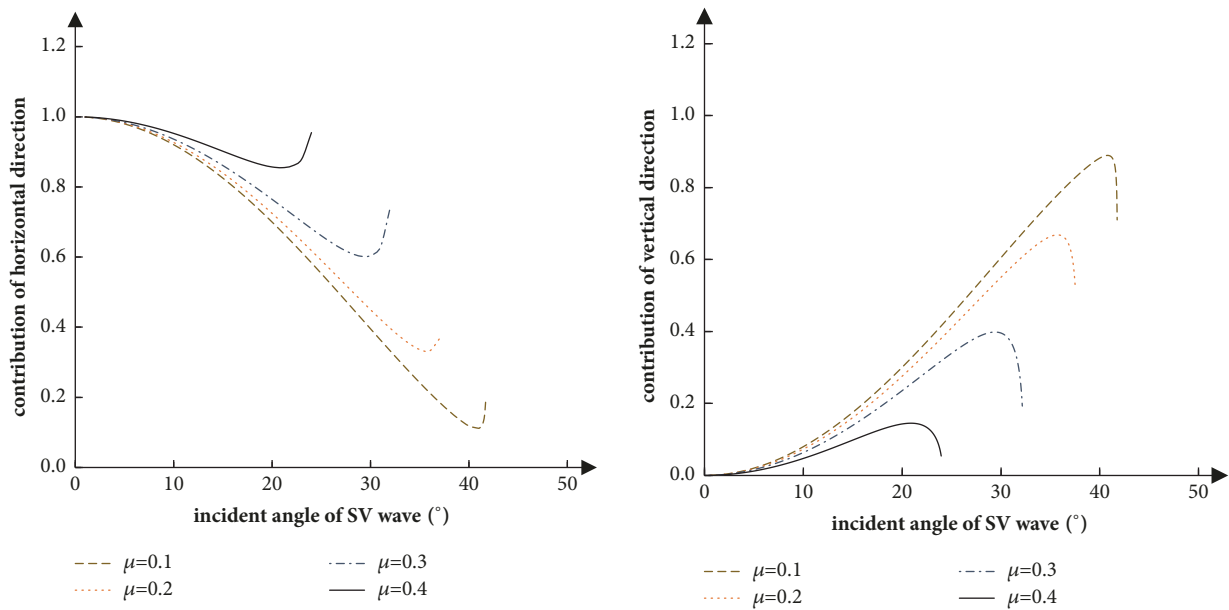


FIGURE 4: Contribution of SV wave to the design ground motion on the free surface.

generally applied to the small incident angle of a plane wave. The viscous boundary has the characteristics of simplicity and directness; however, it has the disadvantage of low-frequency instability and cannot simulate the resilient-elasticity recovery of foundation. The viscous-spring artificial boundary not only is very efficient and convenient to incorporate the reflected waves with existing FEM code but also avoids the numerically unstable phenomena in high and low frequency. And it has a high computational accuracy to simulate the radiation damping [23].

4.1. The Viscous-Spring Artificial Boundary. The viscous-spring artificial boundary consists of elastic springs and dashpots to simulate the influence of the infinite medium to the near field as shown in Figure 5.

The thought of plane waves and scattered waves mixing transmission was put forward by Du et al. [23]. The geometric attenuation of the far-field scattering wave and linear elastic medium of constitutive relation can be taken into account. The 2D and 3D viscous-spring artificial boundaries are expressed as follows, respectively [13].

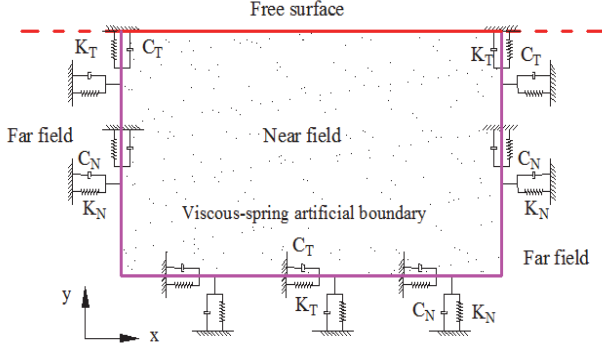


FIGURE 5: The viscous-spring boundary model.

$$K_N = \frac{1}{1+A} \frac{\lambda + 2G}{2^\theta R}, \quad (15)$$

$$C_N = B\rho v_p$$

$$K_T = \frac{1}{1+A} \frac{G}{2^\theta R}, \quad (16)$$

$$C_T = B\rho v_s$$

where K_N and K_T are the coefficients of the normal and tangent elastic stiffness, respectively; C_N and C_T are the coefficients of the normal and tangent viscous damping, respectively; ρ is the density of the medium; λ and G are Lamé's constants; v_p and v_s are the velocity of incident P wave and incident SV wave, respectively; R is the distance from the wave source to the artificial boundary; A and B are correction coefficients. When θ is set to 1 and 0, it corresponds to the 2D and 3D viscous-spring boundary, respectively.

4.2. Seismic Input on the Boundary. The wave field of the artificial boundary is always separated into the free field and scattering field to realize the oblique incidence of seismic wave, which can be expressed by

$$u^T = u^S + u^F \quad (17)$$

where u^T is the wave field; u^S is the scattering field; u^F is the free field.

The motion equation of the viscous-spring artificial boundary can be expressed as

$$M_i \ddot{u}_i^T + C_i \dot{u}_i^T + K_i u_i^T = R_i^F + R_i^S \quad (18)$$

where R_i^F and R_i^S are the equivalent stress load of the boundary node i , which are developed by the free field and scattering field, respectively.

The scatter wave entering into the far field can be simulated by the viscous-spring artificial boundary as follows:

$$R_i^S = -K_i u_i^S - C_i \dot{u}_i^S = -K_i (u_i^T - u_i^F) - C_i (\dot{u}_i^T - \dot{u}_i^F) \quad (19)$$

When simulating the free field, the load imposed on the viscous-spring artificial boundary can be expressed by

$$R_i^F = K_i u_i^T + C_i \dot{u}_i^T + \sigma_i A \quad (20)$$

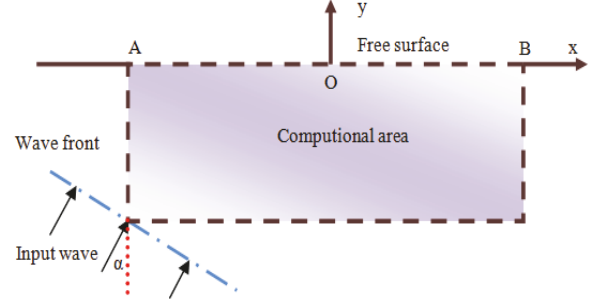


FIGURE 6: Elastic half-space model.

The external source wave motion is treated as the free field and applied to the viscous-spring artificial boundary by converting into stress directly. Interaction force of the artificial boundary under the earthquake effect can be expressed as [13, 24]

$$F_i = K_i u_i^f + C_i \dot{u}_i^f + \sigma_i^f n \quad (21)$$

where i is the node on the artificial boundary; n is the outside normal direction vector on the boundaries; K_i and C_i can be computed by (15) and (16), respectively.

5. Numerical Verification

5.1. The Elastic Half-Space Model Analysis. The half-space model is used to validate the correctness of the oblique incidence method proposed above. Figure 6 shows the model with a depth of 200 m and a width of 840 m. The homogeneous isotropic linear soil half-space model is chosen with the shear modulus $G = 5.292$ GPa, the density $\rho = 2700$ kg/m³, and Poisson's ratio $\mu = 0.25$.

The horizontal and vertical components of the design seismic wave are expressed by (22) and (23), respectively. Figures 7 and 8 show the horizontal and vertical time histories of the displacement and velocity, respectively.

$$u_x(t) = \begin{cases} \sin 4\pi t & 0 \leq t \leq 0.5 \\ 0 & 0.5 < t \leq 2.0 \end{cases} \quad (22)$$

$$u_y(t) = \begin{cases} 2 \sin(4\pi t) - \sin(8\pi t) & 0 \leq t \leq 0.5s \\ 0 & t \geq 0.5s \end{cases} \quad (23)$$

Two components of design ground motion are decomposed by the method presented above, and the oblique plane P and SV waves are input simultaneously at the artificial boundaries. When the angle of incident SV wave is 15°, the corresponding angle of incident P wave is 25°. Figure 9 shows the displacement time histories of typical points A, O, and B on the free surface (Figure 6) compared with the analytic solutions.

When the two components of the input ground motion are different, the displacement responses of typical points A, O, and B on the free surface are similar to the input design

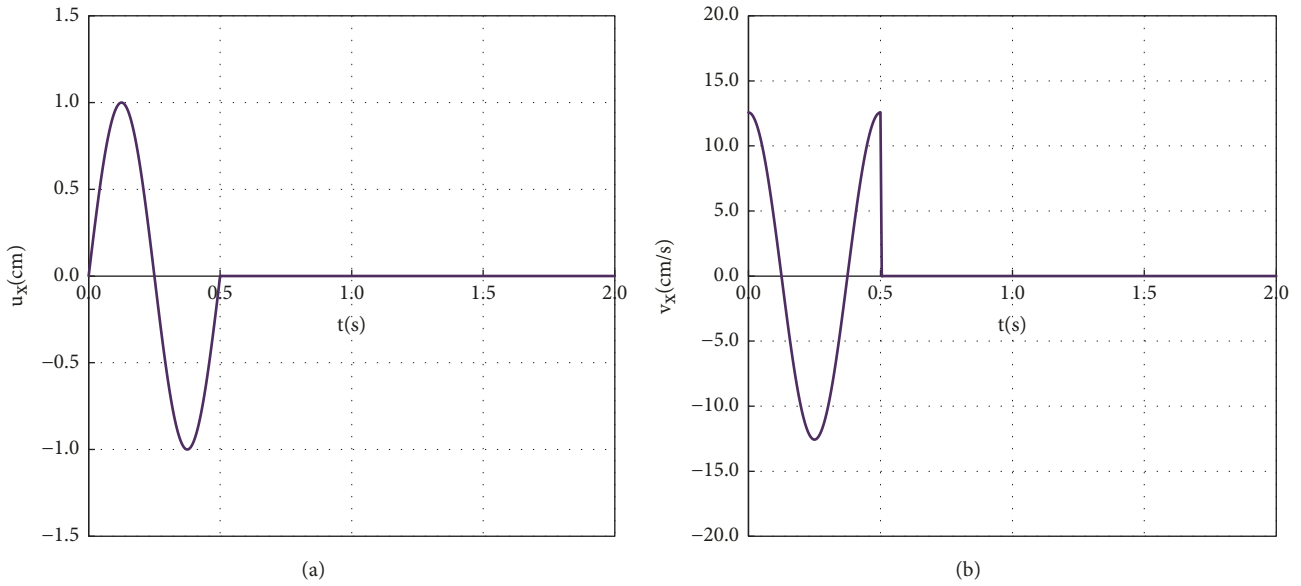


FIGURE 7: Time histories of horizontal design ground motion: (a) displacement and (b) velocity.

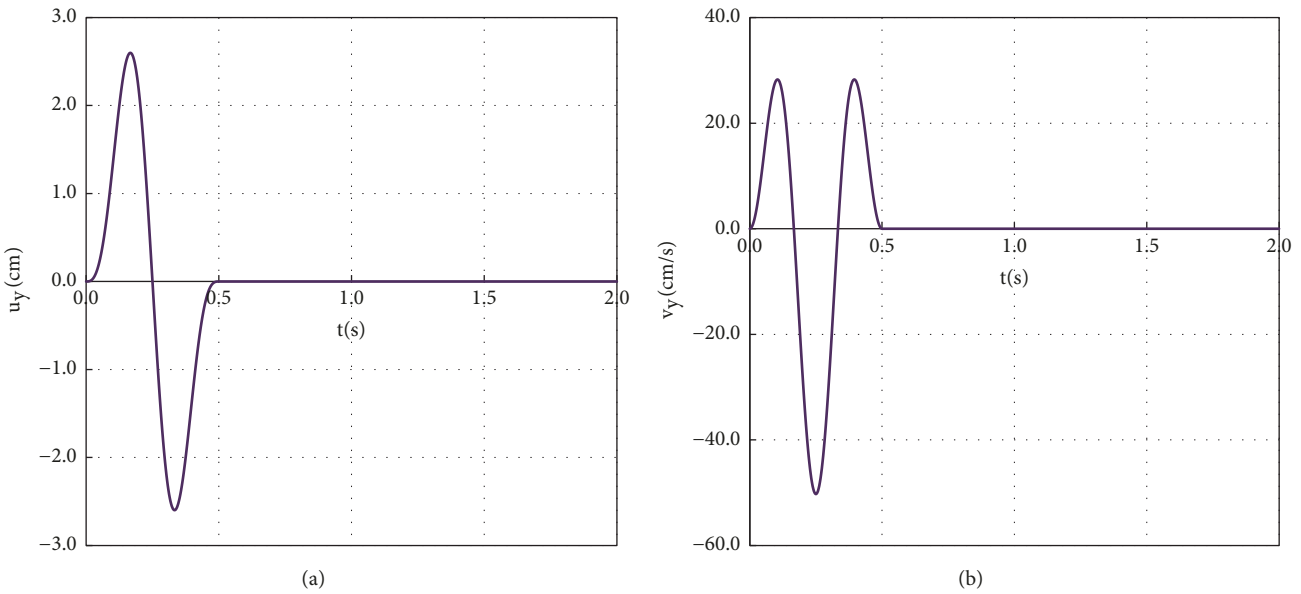


FIGURE 8: Time histories of vertical design ground motion: (a) displacement and (b) velocity.

ground motion as shown in Figure 9, which validates the effectiveness of the method proposed above. The nonuniform ground motion is observed on the free surface because the ground motion occurs at different times.

In order to further analyze the seismic response of the model, the strong ground motion records in Taft earthquake (California) in 1952 are used. Figures 10 and 11 show the time histories of velocity and displacement, respectively.

When the angle of incident SV wave is 30° , the corresponding angle of incident P wave is 54.74° . The oblique incident P wave and SV wave are input simultaneously to obtain the displacement of the typical points A, O, and B on the free surface (Figure 6). The horizontal displacement of the

typical point O compared with the analytic solution is shown in Figure 12(a). The horizontal displacements of the typical points A and B are shown in Figure 12(b). As in the case of the horizontal displacement of the typical points, the vertical displacements are shown in Figure 13.

As shown in Figures 12 and 13, the displacement of point O coincides with the Taft record as a whole and the displacements of points A and B are consistent. The traveling wave effect is reflected by the difference of occurring time of points A and B on the free surface.

5.2. *Dynamic Response Analysis of An Earth-Rock Dam.* A core wall earth-rock dam located on hard bedrock with a

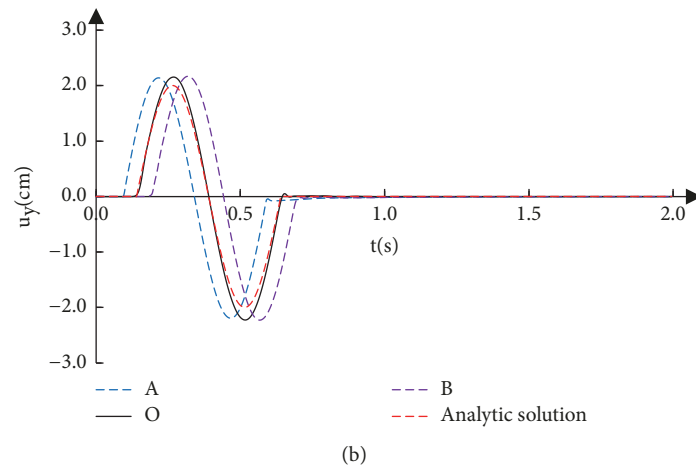
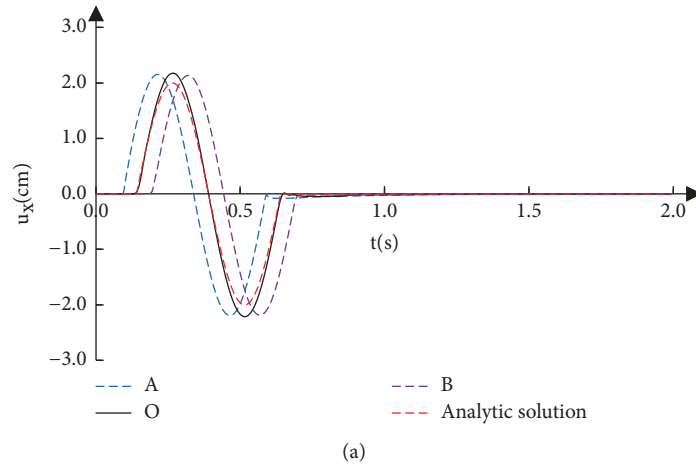


FIGURE 9: Displacement time history of typical points: (a) horizontal and (b) vertical.

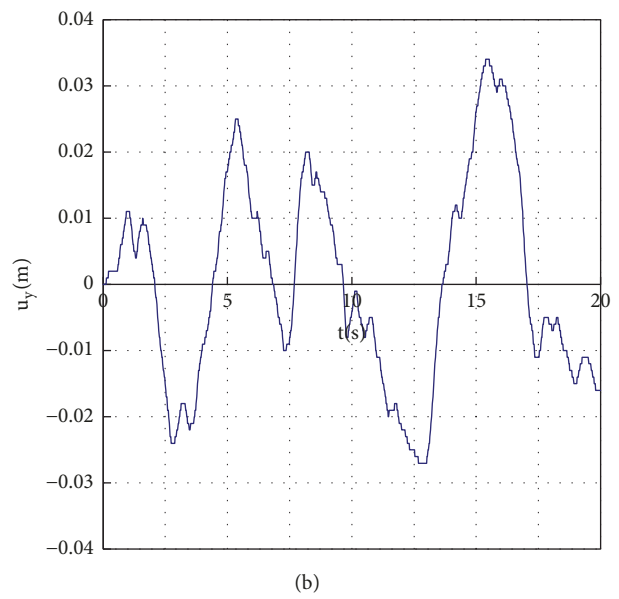
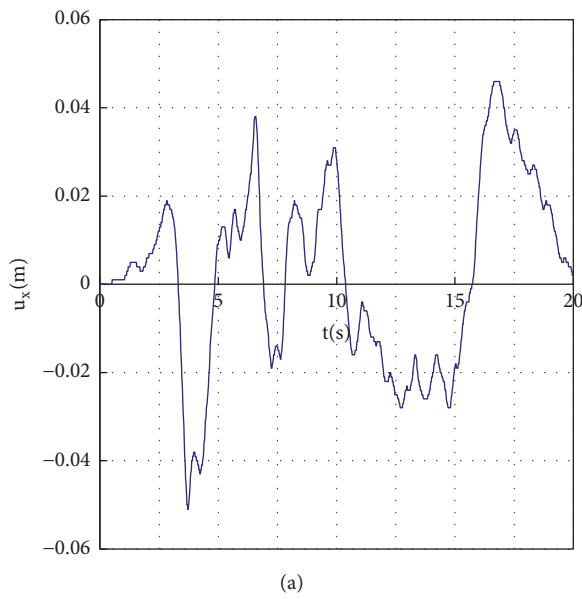


FIGURE 10: Displacement time history of Taft earthquake: (a) horizontal and (b) vertical.

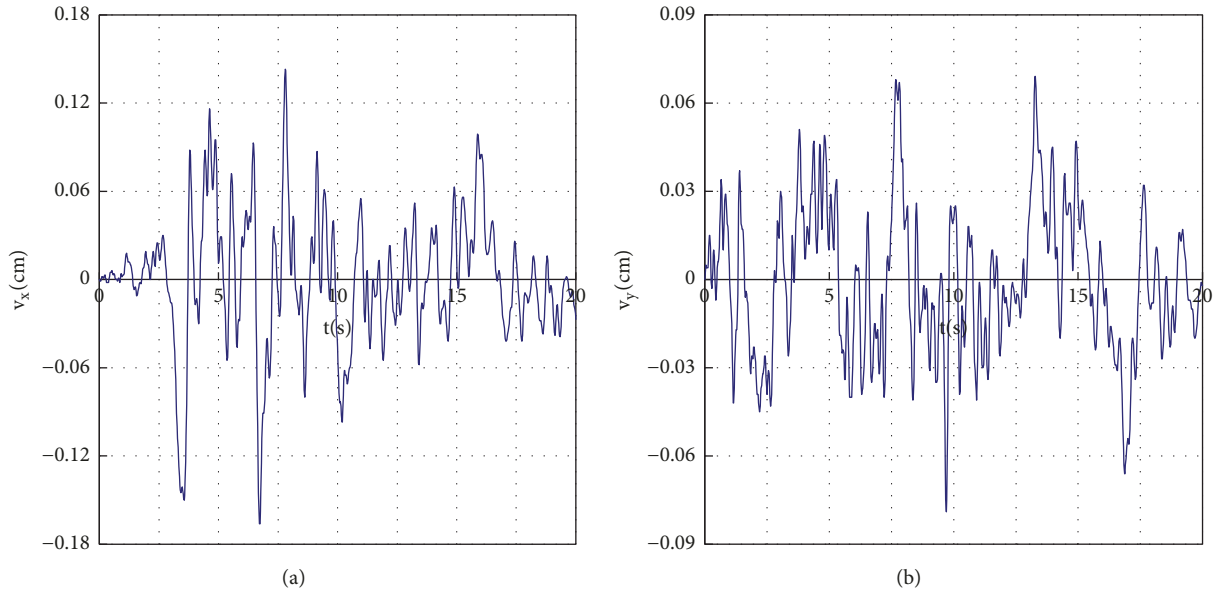


FIGURE 11: Velocity time history of Taft earthquake: (a) horizontal and (b) vertical.

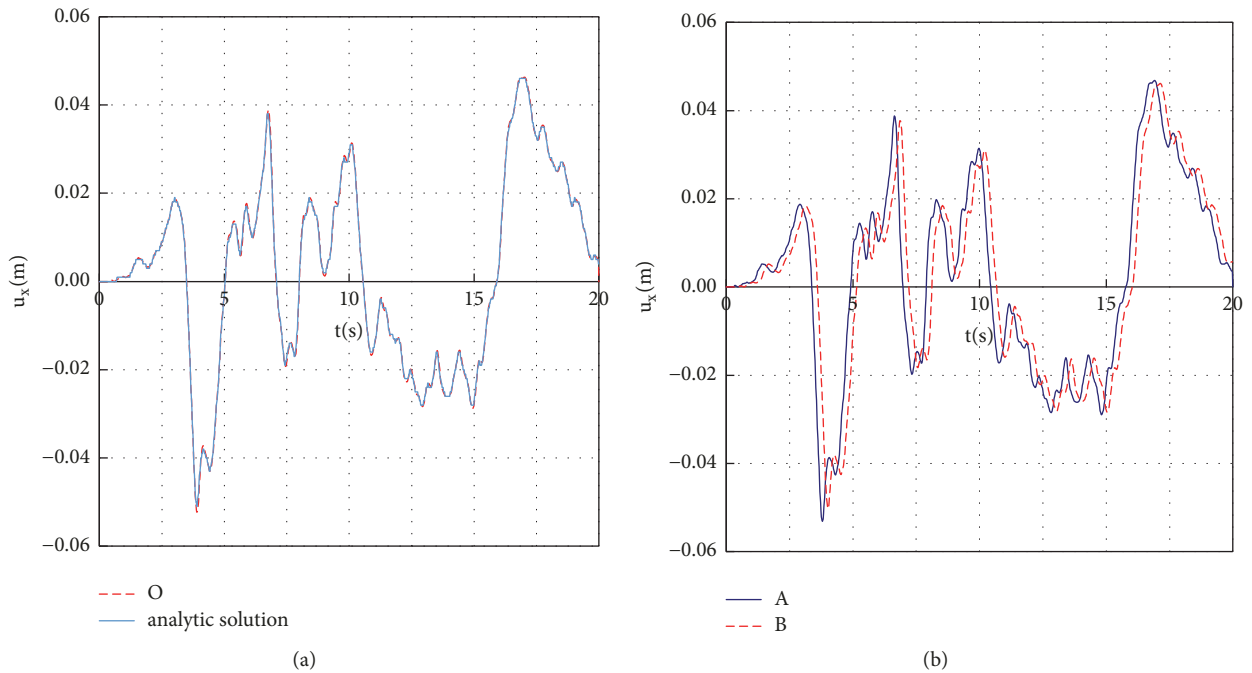


FIGURE 12: Horizontal displacement histories of typical points: (a) point O and (b) points A and B.

height of 100 m is used to study the effect of different incident angle of the input wave. The slope ratios of the upstream and downstream slopes are both 1:2. Figure 14 shows the 2D finite element mesh of the dam. Table 1 lists the parameters of the medium for calculation.

The Taft earthquake records of the first 20 seconds (Figures 10 and 11) are used as the input oblique incident waves. The records of horizontal and vertical waves are treated as two

components of the design seismic wave. The time histories of acceleration and acceleration spectrum are shown in Figures 15 and 16, respectively.

To study and compare the effect of wave incident angle on dam responses, three types of obliquely incident schemes are adopted.

Scheme 1. Seismic waves propagate vertically, and the input angle of wave is 0° .

TABLE I: Calculation parameters.

Material	Density ρ (kg/m ³)	Young's modulus E (Pa)	Poisson's ratio μ
Foundation	2300	2.5×10^{10}	0.2
Dam shell	2000	7.0×10^8	0.3
Core wall	1900	6.1×10^8	0.3

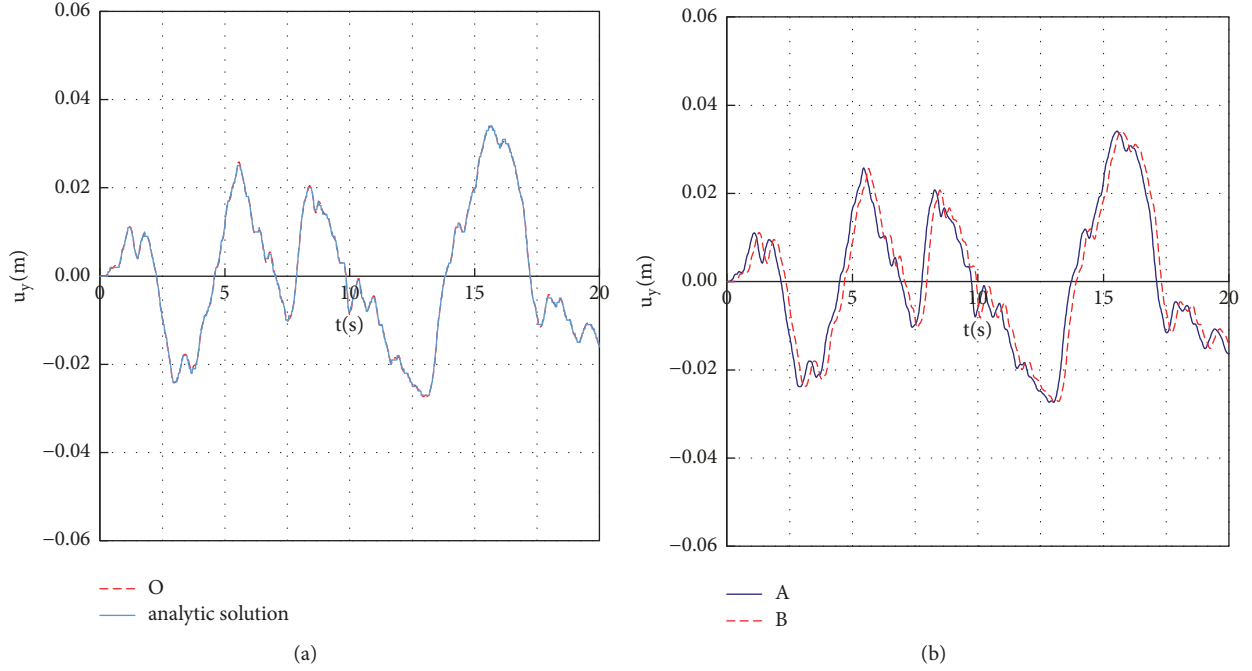


FIGURE 13: Vertical displacement histories of typical points: (a) point O and (b) points A and B.

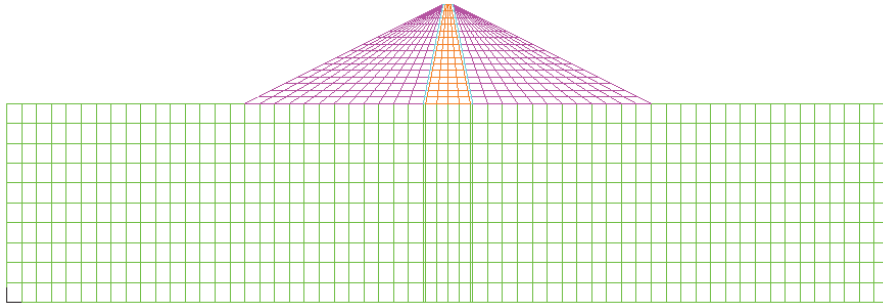


FIGURE 14: Finite element mesh.

Scheme 2. The angle of incidence SV wave is 15° , and the corresponding angle of incidence P wave is 25° .

Scheme 3. The angle of incidence SV wave is 30° , and the corresponding angle of incidence P wave is 54.74° .

5.2.1. Acceleration Distribution. Figures 17–19 show the acceleration distributions of the dam. It can be found that the peak horizontal and vertical accelerations both occur at dam crest. With increasing incidence angle, the acceleration distribution

becomes more asymmetric, and the peak acceleration gradually increases.

5.2.2. Extreme Value of Acceleration and Dynamic Displacement. Extreme values of the acceleration and dynamic displacement of the dam are listed in Tables 2 and 3.

The wave incident angle has a great influence on the dam response according to Tables 2 and 3. With increasing incident angle, the extreme values of acceleration and dynamic displacement gradually increase. Therefore, the

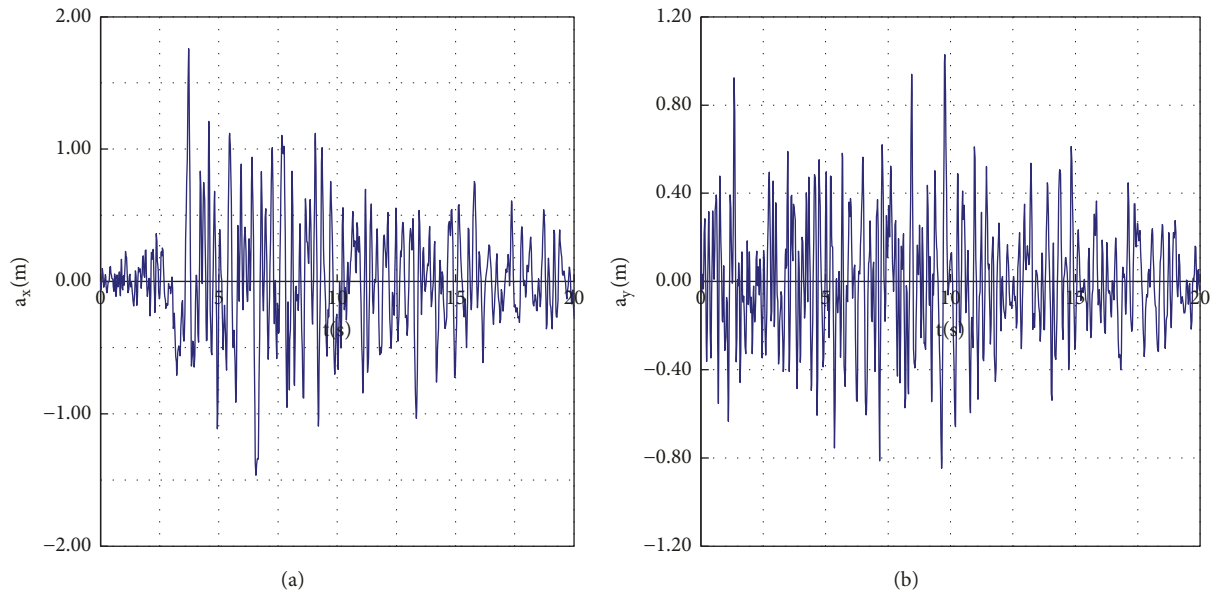


FIGURE 15: Acceleration time histories of Taft earthquake: (a) horizontal and (b) vertical.

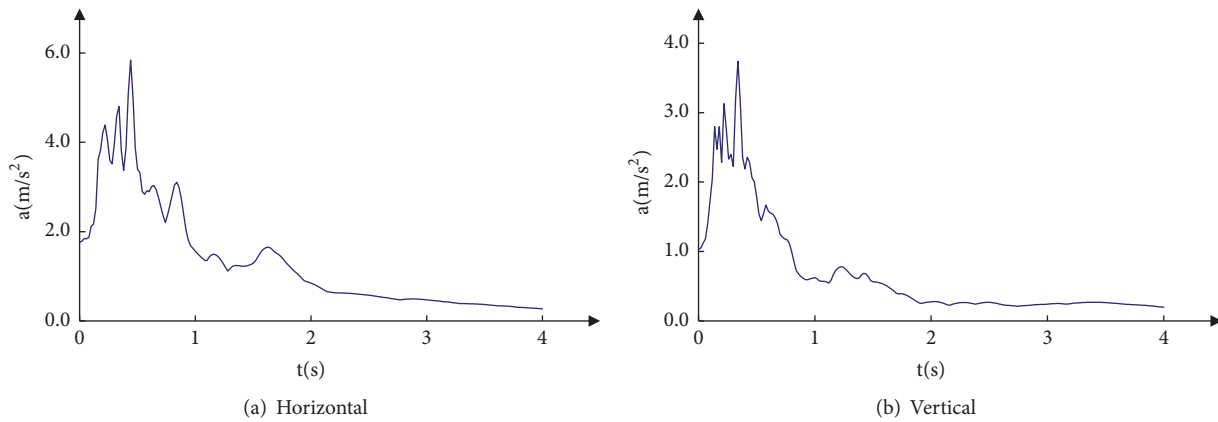


FIGURE 16: Acceleration spectrums of Taft earthquake: (a) horizontal and (b) vertical.

TABLE 2: Extreme value of acceleration (unit: m/s^2).

Direction	Scheme 1	Scheme 2	Scheme 3
Horizontal	6.332	7.177	7.472
Vertical	5.203	5.985	6.333

TABLE 3: Extreme value of dynamic displacement (unit: cm).

Direction	Scheme 1	Scheme 2	Scheme 3
Horizontal	7.6	9.3	9.1
Vertical	3.2	5.3	5.4

seismic response of the dam under the oblique incidence of a seismic wave is much more complicated than that under the normal incidence.

5.2.3. *Comparison of the Peak Dynamic Response of Key Parts of the Dam.* The dynamic response of the dam under the oblique incident wave is obviously different from the case of normal incidence, as shown in Tables 4 and 5. The

extreme values of acceleration and dynamic displacement of the dam are significantly greater than the extremes for normal incidence. The effect of wave incident angle on the top part of the dam body is more serious than other parts of the dam. The extreme values of acceleration and dynamic displacement are the biggest at the downstream crest. Thus, the downstream crest should be especially considered for the seismic design.

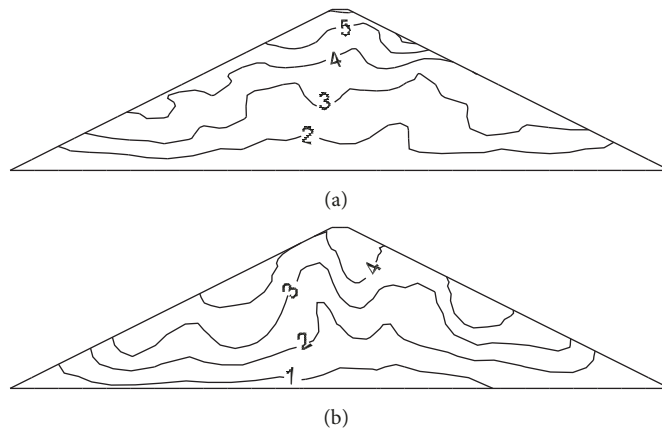


FIGURE 17: Acceleration distribution for Scheme 1 (unit: m/s^2): (a) horizontal and (b) vertical.

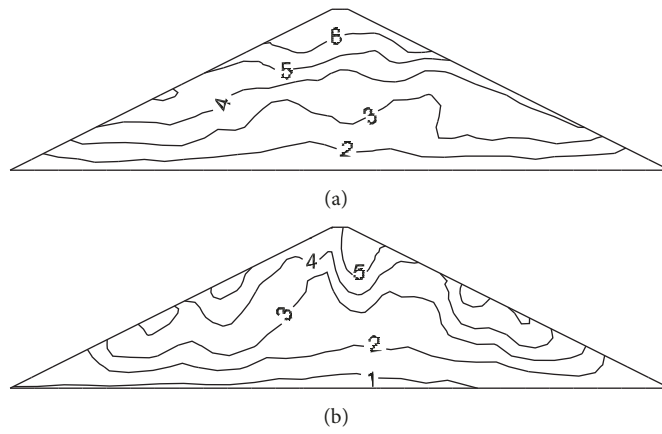


FIGURE 18: Acceleration distribution for Scheme 2 (unit: m/s^2): (a) horizontal and (b) vertical.

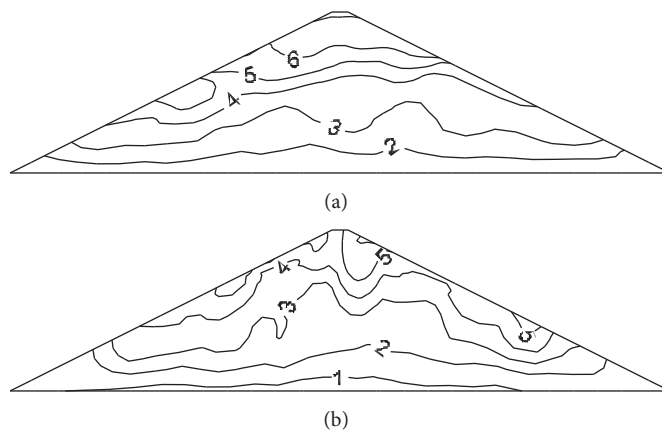


FIGURE 19: Acceleration distribution for Scheme 3 (unit: m/s^2): (a) horizontal and (b) vertical.

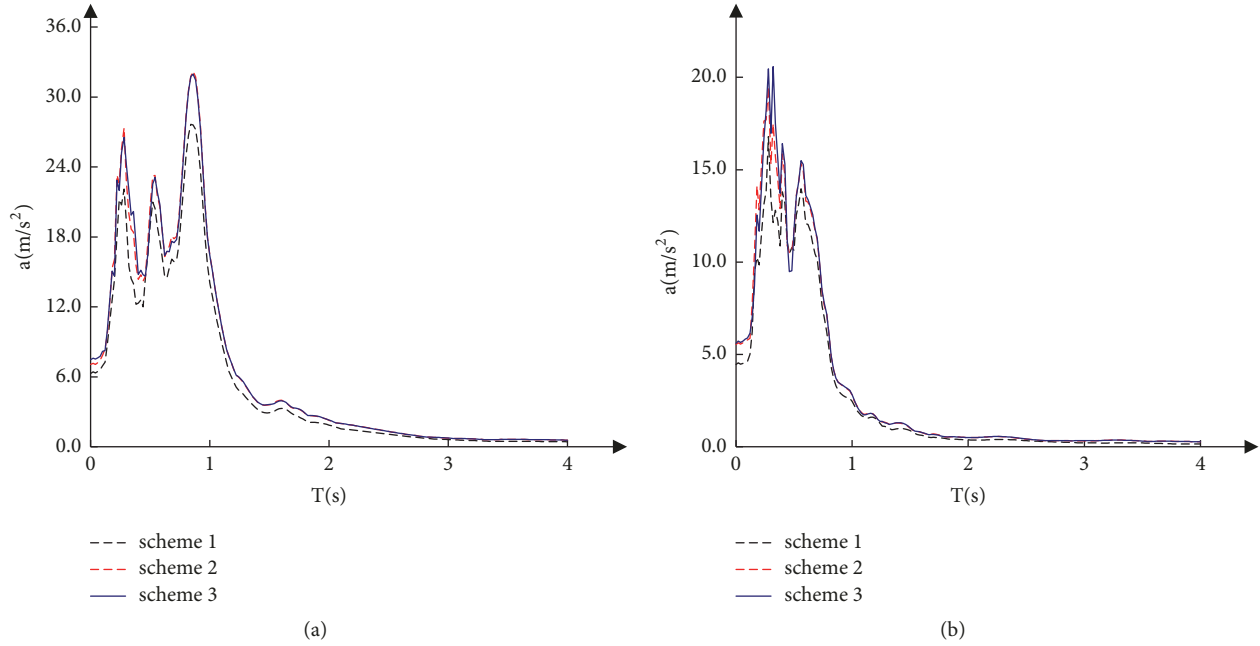


FIGURE 20: Acceleration spectrums of downstream dam crest: (a) horizontal and (b) vertical.

TABLE 4: Acceleration extremums of key parts of the dam (unit: m/s^2).

Location	Direction	Incidence schemes		
		Scheme 1	Scheme 2	Scheme 3
Upstream crest	Horizontal	6.107	7.049	7.425
	Vertical	4.347	3.993	4.885
Downstream crest	Horizontal	6.277	7.069	7.472
	Vertical	4.457	5.538	5.593
Upstream toe	Horizontal	1.320	1.569	1.494
	Vertical	0.852	0.993	1.029
Downstream toe	Horizontal	1.257	1.562	1.534
	Vertical	1.003	1.116	1.085

Figure 20 shows the acceleration spectrum of the downstream crest. The amplitude of spectral acceleration is influenced by the incidence angle. The amplitudes of spectral acceleration of Schemes 2 and 3 are greater than that of Scheme 1, but there is no significant increase between Schemes 2 and 3 from Figure 20(a). The amplitude of acceleration spectrum increases more obviously with the incidence angle as shown in Figure 20(b).

5.2.4. Traveling Wave Effect. Figures 21 and 22 show the acceleration histories at the dam crest and dam toe for seismic wave incident Scheme 3, respectively.

The maximum acceleration at downstream crest is greater than that of the upstream crest for Scheme 3. It can be seen that there is a small phase difference for the acceleration at dam crest in Figure 21, while in Figure 22 there is a significant phase difference for the acceleration at dam toe, which indicates that the nonuniform motion is produced by the oblique incident waves.

6. Conclusions

(1) Based on the assumption that the design seismic components are superposed by oblique P wave and oblique SV wave, this study provided a wave input method considering the obliquely incident waves. The produced seismic response is the same as the design seismic component on the free surface of half-space which validates the effectiveness of the proposed method.

(2) In this study, the time-domain calculation model is established and the free field is simulated to achieve the seismic wave input using the viscous-spring boundary. Numerical simulation of a two-dimensional half-space model is conducted to verify the correctness of the calculation model. The calculation results show that the method can reflect the nonuniform characteristics of seismic waves and has high precision.

(3) Seismic response analysis of an earth-rock dam shows that oblique incidence of seismic waves has a significant

TABLE 5: Dynamic displacement extremums of the dam (unit: cm).

Location	Direction	Incidence schemes		
		Scheme 1	Scheme 2	Scheme 3
Upstream crest	Horizontal	7.6	9.2	9.2
	Vertical	2.8	5.1	5.2
Downstream crest	Horizontal	7.6	9.2	9.2
	Vertical	2.6	4.9	5.1
Upstream toe	Horizontal	3.0	4.6	4.7
	Vertical	1.6	3.4	3.4
Downstream toe	Horizontal	2.9	4.6	4.6
	Vertical	1.6	3.4	3.4

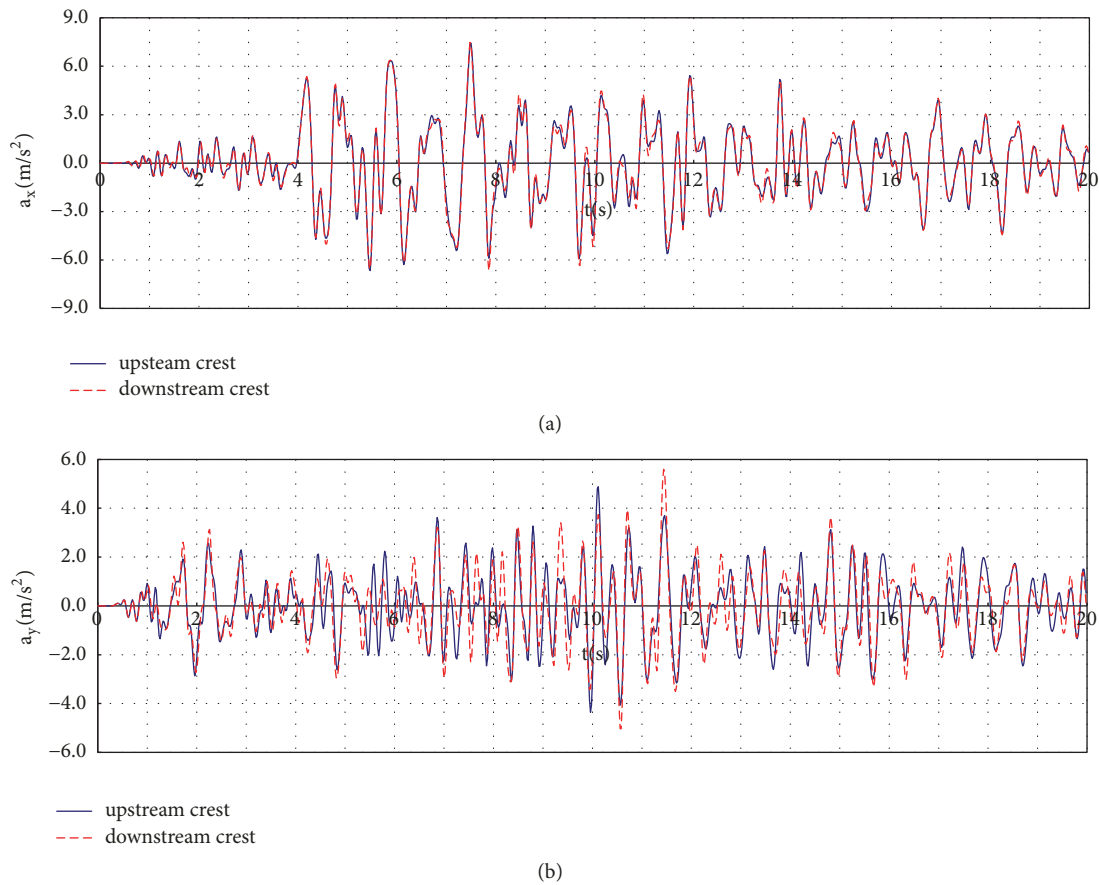


FIGURE 21: Time histories of acceleration at the upstream crest and downstream crest: (a) horizontal and (b) vertical.

influence on the dam, especially for the downstream crest, compared to the case of normal incidence. When the incident angle increases, the seismic response of the dam will be gradually enlarged. It is important for the seismic design of large-scale structures to consider the oblique incidence of the input waves.

Data Availability

The data used to support the findings of this study are available from the corresponding author upon request.

Conflicts of Interest

The authors declare that there are no conflicts of interest regarding the publication of this paper.

Acknowledgments

This work was supported by the CRSRI Open Research Program (Grants nos. CKWV2016376/KY and CKWV2012307/KY), the National Natural Science Foundation of China

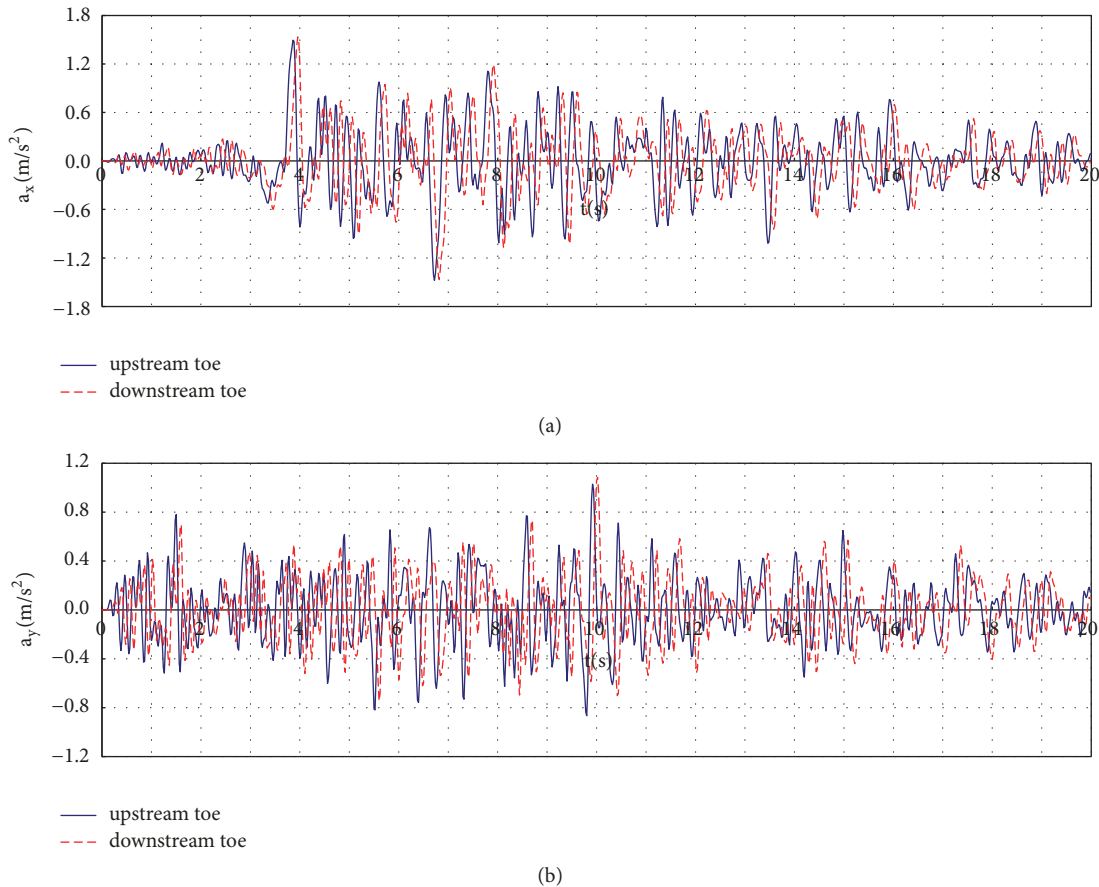


FIGURE 22: Time histories of acceleration at the upstream toe and downstream toe: (a) horizontal and (b) vertical.

(Grant no. 511009055), and the Priority Academic Program Development of Jiangsu Higher Education Institutions.

References

- [1] A. K. Chopra, "Earthquake Response of Earth Dams," *Journal of the Soil Mechanics and Foundations Division*, vol. 93, pp. 65–81, 1963.
- [2] W. J. Cen, L. S. Wen, Z. Q. Zhang, and K. Xiong, "Numerical simulation of seismic damage and cracking of concrete slabs of high concrete face rockfill dams," *Water Science and Engineering*, vol. 9, no. 3, pp. 205–211, 2016.
- [3] Y. Zhao, X. L. Du, and L. Y. Li, "The Effect of Obliquely Incident Seismic Waves on Dynamic Response of Underground Structures," *Journal of Disaster Prevention and Mitigation Engineering*, vol. 30, no. 6, pp. 624–630, 2010.
- [4] W. S. Zhao, Z. W. and P. Q. Zheng, "Choice and Implementation of Seismic Wave Input Method in Numerical Calculation for Underground Engineering," *Chinese Journal of Rock Mechanics and Engineering*, vol. 32, no. 8, pp. 1570–1587, 2013.
- [5] X. L. Du, W. Chen, L. Liang, and Y. L. Li, "Preliminary Study of Time-Domain Seismic Response for Underground Structures to Obliquely Incident Seismic Waves," *Technology for Earthquake Disaster Prevention*, vol. 2, no. 3, pp. 290–296, 2007.
- [6] J. F. Zhao, X. L. Du, Q. Han, and L. Y. Li, "An Approach to Numerical Simulation for External Source Wave Motion," *Engineering Mechanics*, vol. 24, no. 4, pp. 52–58, 2007.
- [7] S. Y. Li, Z. P. Liao, and Z. H. Zhou, "Wave Motion Input in Numerical Simulation of Seismic Response for Large-Scale Structure," *Earthquake Engineering and Engineering Vibration*, vol. 21, no. 2, p. 1, 2001.
- [8] J. Liu and Y. Wang, "A 1D time-domain method for in-plane wave motions in a layered half-space," *Acta Mechanica Sinica*, vol. 23, no. 6, pp. 673–680, 2007.
- [9] Z. Y. Wu, *Study of the Worst Seismic Motion Input for Earth-Dam Seismic Stability under the Oblique Incidence Condition*, Institute of Engineering Mechanics China Earthquake Administration, Harbin, 2007.
- [10] S. Y. Li, *Design Earthquake Input for Important Engineering Structure*, Institute of Engineering Mechanics, Harbin, 2000.
- [11] J. W. Yuan, C. B. Du, and Z. M. Liu, "Study on Oblique Wave Input Based on Design Seismic Component," *Journal of Sichuan University*, vol. 42, no. 5, pp. 250–255, 2001.
- [12] J. W. Yuan, C. B. Du, and Z. M. Liu, "Two-Domain Seismic Response for Gravity Dam to Obliquely Incident and Seismic Wave," *Journal of Vibration and Shock*, vol. 30, no. 7, pp. 121–126, 2011.
- [13] X. L. Du, *Theories and methods of wave motion for engineering*, Science Press, Beijing, 2009.
- [14] H. Cao and V. W. Lee, "Scattering and diffraction of plane P waves by circular cylindrical canyons with variable depth-to-width ratio," *European Journal of Obstetrics & Gynecology and Reproductive Biology*, vol. 9, no. 3, pp. 141–150, 1979.

- [15] V. W. Lee and H. Cao, "Diffraction of SV waves by circular canyons of various depths," *Journal of Engineering Mechanics*, vol. 115, no. 9, pp. 2035–2056, 1989.
- [16] J. W. Yuan, *Nonlinear seismic response analysis of high arch dam with joint key*, Hohai university, Nanjing, 2010.
- [17] Z. P. Liao, "Extrapolation non-reflecting boundary conditions," *Wave Motion. An International Journal Reporting Research on Wave Phenomena*, vol. 24, no. 2, pp. 117–138, 1996.
- [18] R. W. Clayton and B. Engquist, "Absorbing side boundary conditions for wave-equation migration.," *Geophysics*, vol. 45, no. 5, pp. 895–904, 1980.
- [19] B. Engquist and A. Majda, "Radiation boundary conditions for acoustic and elastic wave calculations," *Communications on Pure and Applied Mathematics*, vol. 32, no. 3, pp. 314–358, 1979.
- [20] J. Lysmer and R. L. Kuhlemeyer, "Finite dynamic model for infinite media," *Journal of the Engineering Mechanical Division*, vol. 95, no. 4, pp. 859–878, 1969.
- [21] G. A. Costello, "Large deflections of helical spring due to bending," *Journal of the Engineering Mechanical Division*, vol. 103, no. 3, pp. 481–487, 1977.
- [22] A. J. Deeks and F. M. Randolph, "Axisymmetric time-domain transmitting boundaries," *Journal of Engineering Mechanics*, vol. 120, no. 1, pp. 25–42, 1994.
- [23] X. Du, M. Zhao, and J. Wang, "Stress artificial boundary in FEA for near-field wave problem," *Lixue Xuebao/Chinese Journal of Theoretical and Applied Mechanics*, vol. 38, no. 1, pp. 49–56, 2006.
- [24] H. Q. Chen, "Discussion on seismic input mechanism at dam site," *Journal of Hydraulic Engineering*, vol. 37, no. 12, pp. 1417–1423, 2006.



Hindawi

Submit your manuscripts at
www.hindawi.com

